



Cite this: DOI: 10.1039/d0gc00290a

Conversion of ethanol to 1,3-butadiene over high-performance Mg–ZrO_x/MFI nanosheet catalysts *via* the two-step method†

 Xianquan Li,^{a,b} Jifeng Pang,^a Chan Wang,^a Lin Li,^a XiaoLi Pan,^a
Mingyuan Zheng ^{*a,c} and Tao Zhang^a

Mg–Zr/MFI nanosheet (NS) catalysts were prepared by a wet impregnation method for ethanol conversion to 1,3-butadiene (1,3-BD) *via* the two-step method in a dual fixed bed reaction system. Compared with Zr catalysts loaded on MFI(micro) or commercial SiO₂, 16%Zr/MFI(NS) gave the better performance, with 42.3% 1,3-BD selectivity and 60.5% total conversion of ethanol and acetaldehyde. Introducing 1.2 wt% Mg to 16%Zr/MFI(NS) improved the 1,3-BD selectivity to 54.7% at the expense of a 6% drop in the catalytic activity. Reaction conditions imposed remarkable influence on the reaction results. When the reaction was conducted at 350 °C, a WHSV of 1.44 h⁻¹ and a 2 : 1 ratio of ethanol to acetaldehyde, the 1,3-BD selectivity reached 74.6% with 41.5% total conversion. Such high performance over 1.2%Mg–16%Zr/MFI (NS) was maintained well in a 7 day (168 h) run without deactivation. The catalysts were characterized by XRD, N₂ adsorption, UV-Vis, Raman, and infra-red spectroscopy, NH₃-TPD, TEM and TG. The results showed that the Zr species on MFI(NS) are well distributed with the highest dispersion as compared with the microporous MFI and SiO₂ supported Zr catalysts. The Zr species preferentially occupied the silanol nests of MFI(NS) and eliminated the Brønsted acid sites at 4 wt% Zr loading, and afforded abundant Lewis acid sites in the form of Zr(OH)(OSi)₃ when the Zr loading was increased to 16 wt%. As a base site, Mg is inactive for MPVO reduction but slightly active for the aldol condensation of acetaldehyde, both of which are much inferior to that of the Lewis acid sites. The 1.2%Mg–16%Zr/MFI(NS) catalyst with hierarchical structures of meso- and micro-pores, abundant weak Lewis acid sites but nearly no Brønsted acid sites is competent for the two-step ethanol to 1,3-BD conversion process with high activity, selectivity and stability.

Received 23rd January 2020,

Accepted 8th April 2020

DOI: 10.1039/d0gc00290a

rsc.li/greenchem

1. Introduction

1,3-Butadiene (1,3-BD) is widely used as a monomer for the production of a variety of synthetic polymers such as rubbers, resins and elastomers.^{1,2} Boosted by the rapid growth of the world economy, 1,3-BD consumption has continuously increased in the past decade and reached 12 million tonnes in 2018.^{3,4} Nowadays, 1,3-BD is predominantly produced by the extractive distillation of C₄ fractions in the naphtha cracking process for ethylene production, which largely determines the 1,3-BD production.^{5,6} However, with the development of shale

gas exploitation, more ethylene has been produced *via* the ethane dehydrogenation process, which has decreased the demand for naphtha cracking. Moreover, in China, the successful commercialization of the methanol to olefin conversion technology has led to 4.5 million tonnes per year ethylene productivity, accounting for 1/2 of the ethylene production from the naphtha cracking process in China.⁷ Therefore, it is necessary to explore alternative routes for 1,3-BD production beyond the naphtha cracking method, particularly in a renewable way.

Ethanol is the most productive chemical derived from biomass. The rapid development in biotechnology and catalytic technology like methanol conversion to ethanol makes ethanol suitable for use in the synthesis of many important chemicals, including 1,3-BD.^{4,8,9} Generally, there are two typical ways for the catalytic conversion of ethanol to 1,3-BD (ETB). The one-step method, the so-called Lebedev process which was first developed in the 1920s, solely uses ethanol as the feedstock. The other way is the two-step method, *i.e.*, the

^aDalian Institute of Chemical Physics, Chinese Academy of Sciences, Dalian 116023, P.R. China. E-mail: myzheng@dicp.ac.cn

^bUniversity of Chinese Academy of Sciences, Beijing 100049, China

^cDalian National Laboratory for Clean Energy, Dalian 116023,

People's Republic of China

† Electronic supplementary information (ESI) available. See DOI: 10.1039/d0gc00290a

Ostromislensky process, in which ethanol is first dehydrogenated to acetaldehyde which then reacts with ethanol to form 1,3-BD. The widely accepted reaction pathway of ETB involves four reactions as shown in Scheme 1: (1) ethanol dehydrogenation to acetaldehyde, (2) aldol condensation of acetaldehyde, (3) MPVO reduction of crotonaldehyde with ethanol, and (4) dehydration of crotyl alcohol into 1,3-BD.¹⁰ Evidently, this process involves multiple reaction steps and a complex reaction network, and the reaction intermediates are active and apt to undergo side reactions. This makes it difficult to realize high reaction selectivity, which usually varies in the range of 40–75%.^{1,2} Meanwhile, the catalyst stability is poor. The general catalyst regeneration cycle is about 40 h for the one-step process and 144 h for the two-step process.^{3,11} Therefore, developing catalysts with high activity, selectivity, and particularly high stability is of great significance for the renaissance of ETB application.

According to the reaction and deactivation mechanisms of ETB, the catalyst with high availability of active sites and high efficiency of transfer of intermediates and products in the course of the reaction would have outstanding performance. In our previous study, we developed a Li–Zn–Hf catalyst supported on MFI nanosheets (NS), and obtained superior stability and 1,3-BD yield compared to that on microporous zeolite in the one-step ETB process.¹⁰ In view of the notable advantages of the two-step process over the one-step ETB process in terms of the reaction stability, it is more attractive to explore novel high performance catalysts for the former process. Moreover, in the two-step process, the catalyst in the second reactor does not require active sites for ethanol dehydrogenation. Therefore, it is more convenient to identify the active site functions, modulate active sites according to the catalytic behavior, and design high performance catalysts rationally.

In this work, we prepared a Zr catalyst supported on MFI (NS), and compared it with conventional microporous MFI and mesoporous silica supported catalysts in the ETB reaction. Then, Mg was introduced to Zr/MFI(NS) to modulate the acidic properties of the catalyst and enhance the reaction selectivity. According to comprehensive characterization and conditional experiments, the features of MFI(NS) supported catalysts and the function of active sites for the ETB reaction were illus-

trated. The Mg–Zr/MFI(NS) catalyst exhibited outstanding activity, selectivity and stability in a one week run, and accordingly provided a good reference for designing high performance catalysts for the ETB process.

2. Experimental

2.1 Catalyst preparation

A series of $x\text{Mg}-y\text{Zr}/\text{MFI}(\text{NS})$ catalysts were synthesized by an incipient wetness impregnation method. In detail, MFI(NS) was prepared following the method reported previously.¹⁰ Tetrabutylphosphonium hydroxide (TBPOH) was added dropwise into tetraethyl orthosilicate under stirring, followed by deionized water addition. The mixture was stirred for 12 h, and a clear sol with the composition of $1\text{SiO}_2 : 0.3\text{TBPOH} : 10\text{H}_2\text{O} : 4\text{EtOH}$ (mole ratio) was formed. The sol was sealed in a Teflon-lined stainless steel autoclave and heated for 40 h in a pre-heated oven operating at 388 K. Then, the precipitated white powders were collected by filtration and dried at 373 K. The dried sample was calcined at 823 K for 4 h to remove the organics and obtain MFI(NS). Then, MFI(NS) was impregnated with zirconium oxynitrate aqueous solution. After drying at 120 °C overnight, the sample was calcined at 550 °C for 4 h. Then, Mg was introduced to the as-prepared sample by wetness impregnation of magnesium nitrate solution, and then dried and calcined again to obtain $x\text{Mg}-y\text{Zr}/\text{MFI}(\text{NS})$ catalysts. The Mg loading “ x ” varied from 0.48 wt% to 19.2 wt% and the active component Zr loading “ y ” varied from 4 wt% to 24 wt%. Mesoporous SiO_2 and microporous MFI were also used as supports to load Zr and Mg by the incipient wetness impregnation method. The Zr/MFI(NS) and Mg/MFI(NS) catalysts were also prepared by the same method mentioned above, but without the introduction of the second metal. The supports of microporous MFI and MFI nanosheets were synthesized following the method reported in the literature.^{10,12}

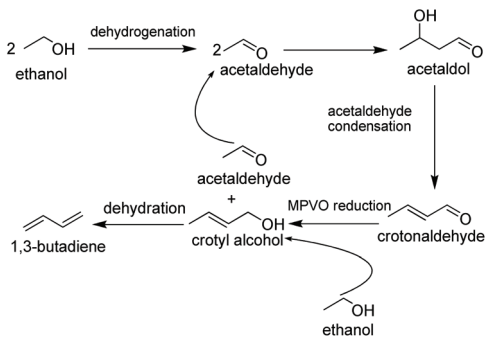
2.2 Catalyst characterization

X-ray diffraction (XRD) patterns of the catalysts were recorded using a PANalytical X'Pert-Pro powder X-ray diffractometer with Cu-K α monochromated radiation ($\lambda = 0.1541 \text{ nm}$) at a scanning speed of 5° min^{-1} in the range of $5\text{--}50^\circ$.

N_2 adsorption and desorption experiments of the catalysts were conducted on a Micromeritics ASAP 2460 system at 77 K. Before measurements, the samples were pretreated at 300 °C for 8 h under vacuum conditions. The specific surface areas were calculated according to the BET equation. The micropore volume, mesopore volume and external surface areas were measured by the t-plot method and the adsorption isotherm was determined by the Barrett–Joyner–Halenda (BJH) method.

Thermogravimetric analysis (TG) was performed on a TA SDTQ600 analyzer at a temperature-programmed rate of $10^\circ \text{ C min}^{-1}$ from room temperature to 800 °C.

The acidity of the catalysts was measured by infra-red spectroscopy of pyridine adsorption using a Bruker Tensor 27 instrument. The samples were pretreated at 350 °C for 1 h in a



Scheme 1 Reaction pathway for the ETB process.

vacuum of 1.0×10^{-2} Pa and then pyridine vapor was introduced at room temperature for 1 min. After that, the pyridine-adsorbed system was heated and evacuated at 150 °C, 250 °C and 350 °C, respectively, and then the spectra were collected at ambient temperature. The acid quantity was calculated by the following equations: C (pyridine on B sites) = $1.88 \text{ IA(B)}R^2/W$, and C (pyridine on L sites) = $1.42 \text{ IA(L)}R^2/W$, where C = concentration (mmol g^{-1}), IA (B or L) = integrated absorbance of B or L bands (cm^{-1}), R = radius of the catalyst disk (cm), and W = weight of the disk (mg).

FTIR of CO adsorption on the catalysts was performed on a Bruker Vertex 70v spectrometer equipped with a DTGS detector. The sample was pretreated at 300 °C for 1 h in a vacuum of 1.0×10^{-5} Pa and then cooled to -173 °C with liquid nitrogen. The FTIR spectra of CO adsorption were collected at different CO pressures, *i.e.*, 0.5, 1, 2, 5 and 10 Torr, respectively.

The acidic properties of the samples were also characterized by NH_3 -TPD on a Micromeritics Autochem II apparatus, equipped with a TCD detector. The catalyst was loaded in a U-shaped fixed-bed quartz microreactor, and pretreated at 300 °C (ramping rate = 10 °C min^{-1}) for 1 h under flowing He (20 mL min^{-1}). When the sample was cooled to 50 °C, 1 mL NH_3 gas was injected with a syringe many times until the saturation of NH_3 adsorption. When the baseline of the TCD signal was stable, the sample was heated to 800 °C at a ramping rate of 10 °C min^{-1} and the TCD signal was recorded.

Transmission electron microscopy (TEM) images, high-angle annular dark-field scanning-transmission electron microscopy (HAADF-STEM) images and energy-dispersive X-ray spectroscopy (EDS) elemental mapping were obtained by using a JEM-2100F microscope, operated at a voltage of 200 kV.

The morphology of the catalysts was observed by scanning electron microscopy (SEM) using a JEOL JSM-7800F microscope.

UV-vis diffuse reflectance spectra of the samples were obtained on a PerkinElmer Lambda 950 spectrometer in the transmittance mode from 200 nm to 800 nm.

Raman spectra of the catalysts were collected with the 523 nm line of the Ne^+ ion laser on Jobin Yvon U-1000.

2.3 Catalyst evaluation

The prepared catalysts were evaluated in a dual fixed bed reaction system. The acetaldehyde–ethanol mixture was produced in the upper reactor to serve as the feedstock for the second fixed-bed reactor. In detail, a flow of N_2 (150 mL min^{-1}) containing ethanol was introduced into the first fixed-bed reactor loaded with 1 g of 20%Cu/SiO₂ catalyst, and heated at 250 °C under atmospheric pressure. After a 24 h on-line induction period for catalyst activation, ethanol was converted to acetaldehyde at *ca.* 96% selectivity and *ca.* 50% conversion. As shown in Fig. S1,† the reaction performance was highly stable in a 200 h run (*ca.* 8 days). Then, the *in situ* generated feedstock stream of an ethanol–acetaldehyde (nearly at a ratio of 1:1) mixture in the N_2 flow entered the second fixed-bed reactor loaded with 1 g of catalyst for the ETB reaction. The

products were analyzed with an online GC (gas chromatograph, Panna GC A91) equipped with a FID detector and a 30 m HP-PLOT Q Column (50 mm \times 30 mm \times 20 mm). The reactants and products including 1,3-BD, ethylene (ELE), ethanol (ETOH), acetaldehyde (ACH), crotonaldehyde (CRH), and diethyl ether (DEE) were quantified.

The conversion and product selectivity (based on the reaction in reactor 2) were calculated according to the following equations:

$$\text{Total conversion (\%)} = (C \text{ mol}_{\text{ethanol tab acetaldehyde}} - (C \text{ mol}_{\text{unreacted ethanol}} + C \text{ mol}_{\text{unreacted acetaldehyde}})) / C \text{ mol}_{\text{ethanol tab acetaldehyde}} \times 100\% \quad (1)$$

$$\text{Ethanol conversion (\%)} = (C \text{ mol}_{\text{ethanol}} - C \text{ mol}_{\text{unreacted ethanol}}) / C \text{ mol}_{\text{ethanol}} \times 100\% \quad (2)$$

$$\text{Acetaldehyde conversion (\%)} = (C \text{ mol}_{\text{acetaldehyde}} - C \text{ mol}_{\text{unreacted acetaldehyde}}) / C \text{ mol}_{\text{acetaldehyde}} \times 100\% \quad (3)$$

$$\text{Product selectivity (\%)} = C \text{ mol}_{\text{product}} / (C \text{ mol}_{\text{ethanol tab acetaldehyde}} - (C \text{ mol}_{\text{unreacted ethanol}} + C \text{ mol}_{\text{unreacted acetaldehyde}})) \times 100\% \quad (4)$$

3. Results and discussion

3.1 Effects of Zr loading on the ETB reaction

Zirconium is a low cost element and has been widely used in catalysts to provide acid sites for the ETB reaction.^{13–15} In this study, Zr was used as the active component for preparing the MFI(NS) supported catalysts.

The performances of Zr-based catalysts at different loadings in ETB were evaluated and are listed in Table 1, entries 1–5. For the blank MFI(NS) support in the ETB reaction, only ethylene and diethyl ether were detected, demonstrating that a number of Brønsted acid sites were present in the zeolite.^{16,17} After inducing 4 wt% Zr to the MFI(NS) support, 1,3-BD was obtained with 10.5% selectivity. Meanwhile, crotonaldehyde, the aldol condensation product, was also produced at a selectivity of 28.1%. Evidently, Zr provides active catalytic sites for aldol condensation and the MPVO reaction. Further increasing the Zr content in the catalyst enhanced the reactant conversion and MPVO reaction, and the highest 1,3-BD selectivity of 37.1% was obtained over 16%Zr/MFI(NS). Thus, 16 wt% Zr was set as the optimal loading on MFI(NS) for further studies in the following sections.

Over the Zr/MFI(NS) catalyst, the selectivity to ethylene and diethyl ether was remarkably lower than that over the blank MFI(NS) support. It is well known that ethanol dehydration reactions are remarkably promoted by the Brønsted acid sites in catalysts.¹⁸ The depressed selectivity to dehydration products over the Zr/MFI(NS) catalyst suggests that the introduction of Zr onto the MFI(NS) support remarkably decreased the

Table 1 Catalytic performance of various Zr catalysts in the ETB process^a

Entry	Catalysts	Conv. (%)			Product selectivity (%)				
		TC	ETOH	ACH	ELE	1,3-BD	DEE	CRH	C-Balance (%)
1	MFI(NS)	7.4	13.7	0.9	79	0	22	0	101
2	4%Zr/MFI(NS)	19.6	29	10.3	12.8	10.5	37.6	28.1	97
3	8%Zr/MFI(NS)	44.2	55.9	32.4	8.8	24.5	9.4	8.3	78.3
4	16%Zr/MFI(NS) ^b	60.5	68.2	52.8	4.9	42.3	3.6	4.9	73.2
5	24%Zr/MFI(NS)	64.7	77.5	55.9	7.4	31.5	3.3	4.9	65.8
6	16%Zr/MFI(micro)	16.2	6.5	25.9	3.6	18.2	9.4	55.4	97.8
7	16%Zr/SiO ₂	55.2	54.6	55.7	4.2	32.8	1.3	5.7	69.1
8	16%Zr/MFI(NS) (450 °C)	61.3	70.3	52.2	4.4	37.1	3.2	2.7	67.8
9	16%Zr/MFI(NS) (650 °C)	57.4	64.3	50.5	5.1	36.4	4.3	4.9	71.7
10	16%Zr/MFI(NS) (750 °C)	51.7	59.1	44.4	6.3	34.4	6.4	5.9	75.7

^a Reaction conditions: $T = 350$ °C, $WHSV = 1.92$ h⁻¹, ethanol : acetaldehyde = 1 : 1. Conv., TC, ETOH, ACH, ELE, 1,3-BD, DEE, CRH and C-balance are abbreviations for conversion, total conversion, ethanol, acetaldehyde, ethylene, 1,3-butadiene, diethyl ether, crotonaldehyde, and carbon balance, respectively. The data were collected after 4 h of reaction. ^b The MFI(NS) support was calcined at 550 °C in entries 1–6.

quantity of acid sites, particularly the Brønsted acid sites. This conjecture was further manifested by the Py-IR spectra of catalysts as discussed in the below context. According to Li and co-workers, when Zr species are loaded on de-Al Beta zeolite, the metal ions preferably locate at the silica nest to form Lewis acid sites.^{19,20} In turn, the number of Brønsted acid sites decreased owing to the adjacent silanols in the nest interacting with Zr to form Si–O–Zr bonds. Therefore, in the MFI(NS) support studied herein, there should also be abundant silanol nests existing, making MFI(NS) versatile to be modified with various transition metals for designing effective catalysts.

In addition, it can be noted that in the presence of Zr species on MFI(NS), the carbon balance was lowered as compared with that of MFI(NS). In view of the reasonably good stability of 24%Zr/MFI(NS) in an 8 h run (Fig. S2†), this should be largely attributed to the formation of undetectable large molecule products from acetaldehyde condensation over the Lewis acid sites on Zr/MFI(NS).

3.2 Effects of the support structure on the ETB reaction

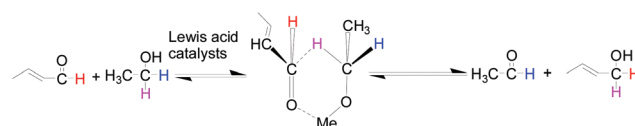
The pore size and structure of catalysts usually impose remarkable influence on the catalytic reactions owing to the mass diffusion and spatial confinement effects.²¹ Herein, three typical supports, *i.e.*, MFI(micro), MFI(NS), and commercial SiO₂, which possess microporous, hierarchical and mesoporous pore structures, respectively, were used to load Zr catalysts for studying the role of the pore structure in the ETB reaction.

Compared to 16%Zr/MFI(NS) with the hierarchical structure (Table 1, entry 4), the microporous MFI supported Zr catalyst showed significantly lower activity for the reactant conversion (16.2% *vs.* 60.5%) and low selectivity to 1,3-BD (18.2% *vs.* 42.3%) in Table 1, entry 6, but with an order of magnitude higher selectivity to crotonaldehyde (55.4% *vs.* 4.9%). This suggests that the MPVO reduction was seriously depressed over the 16%Zr/MFI(micro) catalyst. The conversion of ethanol and acetaldehyde over Zr/MFI(micro) was rather low (6%–26%), also demonstrating that only a small amount of ethanol

was consumed for the MPVO reaction. According to the MPVO mechanism, a six-member ring transition state is involved in the reaction (Scheme 2).^{22–25} In view of the fact that the pore size of MFI(micro) is close to that of the intermediate (0.8 nm *vs.* *ca.* 0.6 nm), it is highly possible that the MPVO reaction is notably prohibited by the spatial hindering effect in the micropores. This leads to the low selectivity of 1,3-BD but high selectivity of crotonaldehyde over 16%Zr/MFI(micro) catalysts. In addition, the micropore structure also hindered the condensation of acetaldehyde due to the less availability of active sites over 16%Zr/MFI(micro).

When commercial mesoporous SiO₂ was used as the support to load Zr sites for the ETB reaction in Table 1, entry 7, the 1,3-BD selectivity and reactant conversion were also inferior to those of 16%Zr/MFI(NS). This suggests that the hierarchical structures of MFI(NS) facilitate the active site dispersion and reactant transportation, and MFI(NS) is a superior support for the ETB conversion.

The thermal stability of MFI(NS) was checked by calcination at different temperatures. There are abundant silanols on the surface of MFI zeolite, and the over-high calcination temperature may cause loss of the quantity of silanol and affect the performance of the catalysts.²⁶ The results listed in Table 1, entries 4, 8–10, show that in a wide range of calcination temperatures (450–750 °C), the MFI(NS) supported Zr catalysts showed similar performances, and MFI(NS) calcined at 550 °C was the relatively optimal one. Evidently, the nanosheets of MFI zeolite are rather stable. This is consistent with the good performance of the regenerated MFI(NS) catalysts as we reported previously.¹⁰



Scheme 2 Mechanism of the MPVO reaction, Me = metal.²²

3.3 Catalytic performance of Mg–Zr/MFI(NS)

The key role of acid–base sites in the Lebedev process, especially in the Mg–Si systems, was extensively investigated.^{27–29} Angelic *et al.* proposed that the balanced acid and base sites with a moderate strength catalyzed the aldol condensation step and depressed the side reactions in the ETB reaction.^{30–32} Thus we introduced base sites of Mg to modulate the acidic properties of Zr/MFI and improve its catalytic performance.

3.3.1 Effects of Mg loading on the ETB reaction over Mg–Zr/MFI(NS) catalysts. The 16%Zr/MFI(NS) catalyst was modified with different amounts of Mg and tested in the ETB reaction. As shown in Table 2, entries 1–5, the activity of Mg–Zr/MFI(NS) catalysts was slightly lower than that of 16%Zr/MFI(NS) after Mg addition. However, the 1,3-BD selectivity was improved, and the highest value of 54.7% was obtained over the 1.2%Mg–16%Zr/MFI(NS) catalyst. At higher loadings of Mg, the total conversions decreased more remarkably, demonstrating that the presence of Mg in the Zr catalysts depressed the ETB reaction. This is quite contrary to some previous arguments that base sites of Mg greatly contribute to condensation of acetaldehyde.³³

In addition, the crotonaldehyde selectivity was enhanced to 32.8% over 19.2%Mg–16%Zr/MFI(NS). Correlating to the lowered conversions of ethanol and acetaldehyde, it can be conjectured that the over-abundant base sites of Mg remarkably depress the MPVO reduction, and lead to a rather large fraction of the condensation product being intact. In another word, the base sites of Mg do not contribute to MPVO reduction.

3.3.2 Catalytic role of Mg in the ETB reaction. To further probe the catalytic role of Mg in the ETB reaction, Mg was loaded on MFI(NS) at different loadings and tested in the reaction. As shown in Table 2, entries 6–8, the Mg introduction to MFI(NS) depressed the dehydration reaction, with ethylene selectivity dropping from 79% to 30%. In contrast to no yield of crotonaldehyde over the blank MFI(NS) support, the condensation product was present over both 1.2%Mg/MFI(NS) and 19.2%Mg/MFI(NS) catalysts. Evidently, the base sites of Mg

really catalyze the condensation reaction. However, the total conversions of ethanol and acetaldehyde over them are rather low (<10%), very close to that over the MFI(NS) support. This demonstrates that the activity of base sites of Mg for the condensation reaction is much lower than that of the acid sites of Zr on 16%Zr/MFI(NS), which gave 60% total conversion and 47% C₄ product selectivity. This is consistent with the results discussed above that the activity of Mg–Zr/MFI(NS) catalysts is generally lower than that of 16%Zr/MFI(NS).

In addition, no 1,3-BD product was obtained over the Mg/MFI(NS) catalyst, suggesting that Mg sites do not catalyze the MPVO reaction. This is also consistent with the conclusion from the performance of 19.2%Mg–16%Zr/MFI(NS) discussed above. Therefore, the major role of Mg in the ETB reaction over Mg–Zr/MFI catalysts lies in subtly tuning the acidity of catalysts so that the rates of condensation and MPVO reactions match well to lead to enhanced 1,3-BD selectivity.

3.4 Reaction condition influence and catalyst stability

Because the ETB process consists of a series of cascade steps which have distinct activation energies, the reaction temperature will drastically affect the rate of the rate-determining step and change the reaction selectivity.

The reaction temperature influence on the reaction was evaluated. As shown in Table 3, entries 1 and 2, when the reaction was conducted at 250–275 °C, crotonaldehyde was obtained at a high level (30–40% selectivity), which overwhelmed the 1,3-BD selectivity (6–24%). Increasing the reaction temperature to 300–375 °C (Table 3, entries 3–6) led to 1,3-BD being changed to the major product. At a higher temperature of 400 °C (Table 3, entry 7), the selectivity to ethylene was enhanced remarkably. These results suggest that the MPVO reaction has a higher apparent activation energy than the aldol condensation over Mg–Zr/MFI catalysts, and 325–350 °C is a favorable temperature range for the high selectivity of 1,3-BD.^{1,13,34}

The reaction space velocity and the ratio of ethanol to acetaldehyde in the feedstock are important factors for the two-step ETB process. We modulated the weight of the catalyst and

Table 2 Effects of Mg–Zr on the catalytic performance in the ETB process^a

Entry	Catalysts	Conv. (%)			Product selectivity (%)				
		TC	ETOH	ACH	ELE	1,3-BD	DEE	CRH	C-Balance (%)
1	16%Zr/MFI(NS)	60.5	68.2	52.8	4.9	42.3	3.6	4.9	73.2
2	0.48%Mg–16%Zr/MFI(NS)	53.6	59.4	47.8	8.2	46.6	6.0	5.3	81.8
3	1.2%Mg–16%Zr/MFI(NS)	54.1	56.2	52.1	4.6	54.7	4.8	5.6	83.7
4	4.8%Mg–16%Zr/MFI(NS)	36.5	32.2	40.9	4.7	43.4	4.7	8.3	85.8
5	19.2%Mg–16%Zr/MFI(NS)	21.2	29.3	29.3	8.3	50.4	11.5	32.8	100
6	MFI(NS)	7.4	13.7	0.9	79	0	22	0	100
7	1.2%Mg/MFI(NS)	9.8	6.9	12.7	31.2	0	36.8	8.7	97.7
8	19.2%Mg/MFI(NS)	9.7	8.1	11.2	30.3	0	21.6	20.7	97.3
9	1.2%Mg–16%Zr/MFI(NS) ^b	49.3	57.6	40.9	6.4	40.4	6.5	6.5	80.3

^a Reaction conditions: $T = 350$ °C, WHSV = 1.92 h⁻¹, ethanol : acetaldehyde = 1 : 1. Conv., TC, ETOH, ACH, ELE, 1,3-BD, DEE, CRH and C-balance are abbreviations for conversion, total conversion, ethanol, acetaldehyde, ethylene, 1,3-butadiene, diethyl ether, crotonaldehyde, and carbon balance, respectively. ^b The Mg precursor is magnesium acetylacetonate.

Table 3 Reaction results over 1.2%Mg–16%Zr/MFI(NS) under different conditions^a

Entry	Reaction conditions	Conv. (%)			Product selectivity (%)				
		TC	ETOH	ACH	ELE	1,3-BD	DEE	CRH	C-Balance (%)
1	250 °C, 1.92 h ⁻¹ , E/A = 1 : 1	21.5	19.2	23.6	1.2	6.2	4.2	29.5	87.4
2	275 °C, 1.92 h ⁻¹ , E/A = 1 : 1	19.5	16	23.5	1.9	24.2	5.5	41.5	94.8
3	300 °C, 1.92 h ⁻¹ , E/A = 1 : 1	23	20	26.2	4.7	46.2	8.5	19.2	95.1
4	325 °C, 1.92 h ⁻¹ , E/A = 1 : 1	34.7	34.7	34.7	4.9	37.1	5.8	9.3	85.1
5	350 °C, 1.92 h ⁻¹ , E/A = 1 : 1	54.1	56.2	56.2	4.6	54.7	4.8	5.6	73.2
6	375 °C, 1.92 h ⁻¹ , E/A = 1 : 1	63.8	75.5	75.7	12.3	34.4	4.8	4.3	71.8
7	400 °C, 1.92 h ⁻¹ , E/A = 1 : 1	64.5	78.8	78.8	25.7	39.3	5.3	4.5	83.8
8	350 °C, 0.96 h ⁻¹ , E/A = 1 : 1	60.7	54.1	67.3	4.8	62.5	4.5	5.9	86.5
9	350 °C, 1.44 h ⁻¹ , E/A = 2 : 1	41.5	30.1	64.4	7	74.6	8.4	5.4	97.9
10	350 °C, 1.92 h ⁻¹ , E/A = 3 : 1	28.1	18.1	56	3.3	70.3	4.7	6.1	95.6

^a Reaction conditions: $T = 250\text{--}350\text{ }^{\circ}\text{C}$, $\text{WHSV} = 0.96\text{--}1.92\text{ h}^{-1}$, ethanol : acetaldehyde = 1 : 1–3 : 1. Conv., TC, ETOH, ACH, ELE, 1,3-BD, DEE, CRH and C-balance are abbreviations for conversion, total conversion, ethanol, acetaldehyde, ethylene, 1,3-butadiene, diethyl ether, crotonaldehyde, and carbon balance, respectively. E/A represents the ratio of ethanol to acetaldehyde.

the ethanol feeding rate to change the WHSV and feedstock composition, and the reaction results over 1.2%Mg–16%Zr/MFI(NS) are listed in Table 3, entries 8–10. Although the effect of E/A on 1,3-BD selectivity cannot be identified exactly because of the E/A and the reaction WHSV being concurrently changed in our experiments, the E/A ratio at 2–3 seems to favor 1,3-BD production, which is well consistent with the results over Ta₂O₅/SiO₂ discussed previously.¹ When the reaction was conducted at 350 °C, a WHSV of 1.44 h⁻¹ and a 2 : 1 ratio of ethanol to acetaldehyde, the 1,3-BD selectivity reached 74.6% with 41.5% ethanol and acetaldehyde conversion. Under these optimal conditions, the catalyst stability was evaluated. As shown in Fig. 1, the catalytic performance was well maintained in a one-week run. The 1,3-BD selectivity fluctuated between 70–80% and the total conversion of ethanol and acetaldehyde was maintained at *ca.* 40%. Compared to the results in the literature, the performance of 1.2%Mg–16%Zr/

MFI (NS) is rather attractive in view of the high yield of 1,3-BD, relatively mild reaction conditions and high stability.^{3,14,16,35,36} The TG analysis of the spent catalyst shows that there is merely 12 wt% carbonaceous deposition on the catalyst after a seven day run (Fig. S3†). This should be attributed to the MFI nanosheet structure and abundant active sites of Mg and Zr in the catalyst.

3.5 Catalyst characterization

To reveal the high performance and stability of MFI(NS) supported Mg–Zr catalysts, the catalyst texture and acidic properties were characterized and correlated to the reaction results.

3.5.1 Zr dispersion on the catalysts. The dispersion of Zr on different silica supports was investigated using the XRD pattern shown in Fig. S4.† No peaks owing to crystalline ZrO₂ particles were observed over MFI(NS), MFI(micro) and SiO₂ supported catalysts, suggesting the uniform distribution of the ZrO₂ component. Specifically, Zr species on MFI(NS) were highly dispersed, as evidenced from the TEM and HAADF-STEM images and EDS mapping results in Fig. S5.†

The Zr dispersion on the supports was further studied by using UV-vis diffuse reflectance spectra shown in Fig. 2. The absorbance of bulk ZrO₂ was around 230–240 nm, ascribed to the octahedral coordination state as reported in the literature.^{37,38} For the supported Zr catalysts, a substantial blue shift in the absorbance was observed particularly on 16% Zr/MFI(NS). The adsorption bands at 205–215 nm may be attributed to the ligand-to-metal charge transfer (LMCT) from an O²⁻ ion to an isolated Zr⁴⁺ ion in a tetrahedral configuration.^{37–39} According to Li and coworkers, the loading of Zr on de-Al Beta zeolite formed the tetrahedrally coordinated framework Zr species which acted as Lewis acid centers for the reactions.²⁰ However, considering the difference in the structure of MFI(NS) and de-Al Beta zeolites, it is still not safe to regard that Zr⁴⁺ ions stay in MFI(NS) in a tetrahedral configuration just based on the UV-vis analysis. Over Zr/MFI(micro), a small shoulder at *ca.* 230 nm was observed,

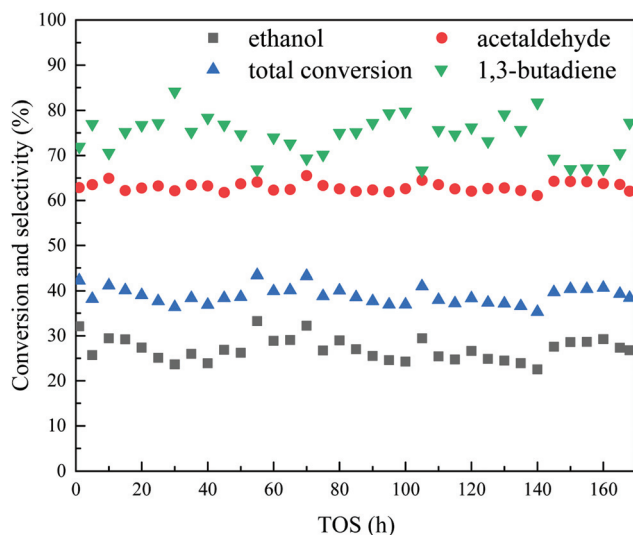


Fig. 1 Stability of 1.2%Mg–16%Zr/MFI(NS) in the ETB reaction (reaction conditions: $T = 350\text{ }^{\circ}\text{C}$, $\text{WHSV} = 1.44\text{ h}^{-1}$, ethanol : acetaldehyde = 2 : 1).

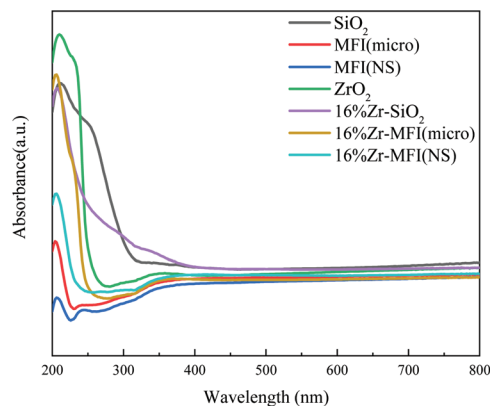


Fig. 2 UV-Vis diffuse reflectance spectra of different supports and Zr-based catalysts.

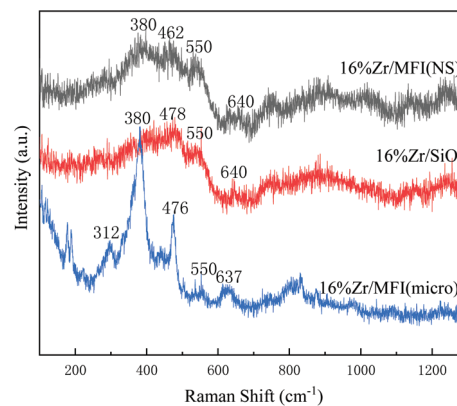


Fig. 4 Raman spectra of Zr on different supported catalysts.

indicating that nanoscopic regions of Zr–O–Zr linkages were formed on the microporous MFI supported catalyst. The absorbance edge was converted to the absorbance band edge energy following the equation: $ah\nu = A(h\nu - E_g)^{1/2}$, where α is the absorbance intensity at a light frequency of ν , A is the absorbance constant and E_g is the absorbance edge energy. As shown in Fig. 3, the absorbance edge energies of Zr for bulk ZrO_2 , MFI(micro), SiO_2 and MFI(NS) supported Zr catalysts are 4.8, 5.0, 5.2 and 5.4 eV, respectively. The higher absorbance edge energies of the Zr catalysts can be ascribed to the LMCT from O^{2-} to Zr^{4+} with lower coordination, due to the formation of Zr–O–Si and Zr–OH linkages.³⁹ The energies increase in the order of 16%Zr/MFI(micro) < 16%Zr/ SiO_2 < 16%Zr/MFI(NS), suggesting that the Zr oxide on MFI(NS) has the highest dispersion while Zr/MFI(micro) has the lowest. This is well consistent with the trend of catalytic performance, where 16%Zr/MFI(NS) behaved the best among the three supported catalysts in the ETB reaction.

Raman spectra provide more information about ZrO_2 dispersion. As shown in Fig. 4, the bands at 380 cm^{-1} of 16%Zr/MFI(micro) should be attributed to the characteristic peak of Si–O bonds in the five membered ring of the MFI-type unit structure.⁴⁰ The bands at 637 cm^{-1} stand for monoclinic ZrO_2

and the bands at 550 and 476 cm^{-1} are ascribed to the three-dimensional amorphous ZrO_2 .³⁷ These bands were hardly found in 16%Zr/ SiO_2 and 16%Zr/MFI(NS) catalysts. This result indicates that over the MFI(NS) and mesoporous silica supported catalysts, ZrO_2 was highly dispersed without bulk ZrO_2 particle formation. This conclusion is consistent with the UV-vis diffuse reflectance spectra results discussed above.

3.5.2 Acidic properties of Mg–Zr/MFI(NS) catalysts. The acidic properties of Mg–Zr catalysts were measured by NH_3 -TPD, Py-IR and CO adsorption. The NH_3 -TPD profiles are shown in Fig. 5; it was found that the Zr/MFI(NS) catalysts have less acid sites compared to the blank MFI(NS) support, and the strength of acidity decreased with the increase of Zr loading on the support. This suggests that Zr introduction onto MFI(NS) weakens the acidity of MFI(NS). This is in agreement with the reaction results listed in Table 1, entries 2–6, where less yields of dehydration products were obtained over Zr/MFI(NS) catalysts compared to the MFI(NS) counterpart.

Py-IR provides quantification information of acid sites. As shown in Fig. 6 and Table 4, no Lewis acid sites but a large number of Brønsted acid sites ($57.8\text{ }\mu\text{mol g}^{-1}$) were present on MFI(NS). After introducing 4% or 16% Zr onto MFI(NS), Lewis acid sites were generated at the expense of Brønsted acid sites.

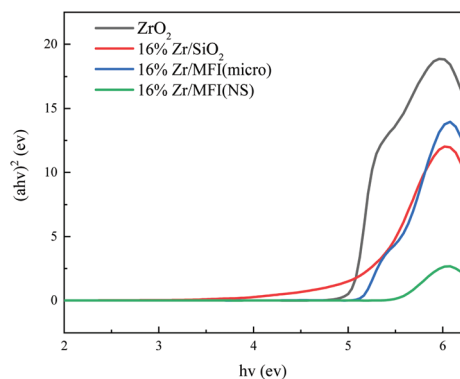


Fig. 3 Plots of $(ah\nu)^2$ versus $h\nu$ of the various catalysts.

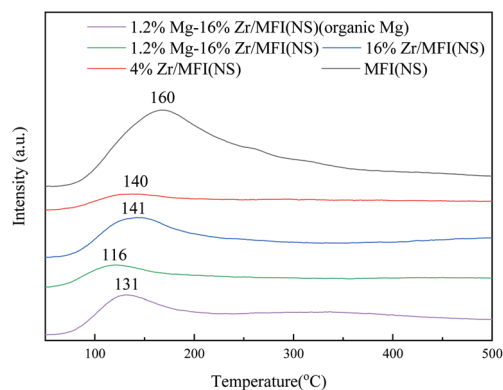


Fig. 5 NH_3 -TPD profiles of MFI(NS) and MFI(NS) supported catalysts.

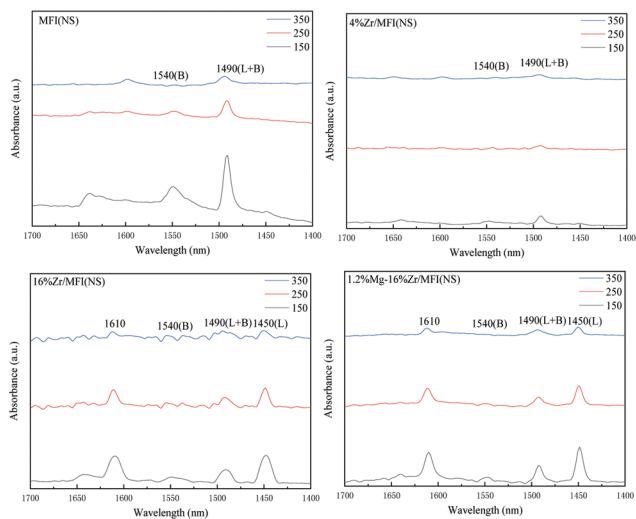


Fig. 6 Py-IR spectra for MFI(NS) and MFI(NS) supported catalysts.

Table 4 Acidic properties of the MFI support and Zr-based catalysts

Catalyst	Lewis acid site number ^a ($\mu\text{mol g}^{-1}$)	Brønsted acid site number ^a ($\mu\text{mol g}^{-1}$)
MFI(NS)	—	57.8
4%Zr/MFI(NS)	2.0	6.0
16%Zr/MFI(NS)	72.0	24.0
1.2%Mg-16%Zr/MFI(NS)	84	11.7
1.2%Mg-16%Zr/MFI(NS) _(organic Mg)	80.3	23.9

^a Lewis acid and Brønsted acid sites were calculated according to the 1450 and 1540 cm^{-1} peak areas, respectively, of pyridine adsorption at 150 °C.

Over 16%Zr/MFI(NS), the number of Lewis acid sites reached 72.0 $\mu\text{mol g}^{-1}$, which is three times that of the Brønsted acid sites. Correlating the reaction results with the acid site properties, it can be found that the proceeding of the ETB reaction majorly depends on the Lewis acid sites, which not only catalyze the aldol condensation between ethanol and acetaldehyde, but also realize the critical MPVO reduction of the intermediate. In contrast, the Brønsted acid sites just facilitate the dehydration to byproducts.

The acid sites on Zr/MFI(NS) were further probed with CO adsorption. As shown in Fig. 7, three typical FTIR bands were observed on the spectra of 16%Zr/MFI(NS) but only two peaks were present for 4%Zr/MFI(NS). According to the report of Ivanova *et al.*, the FTIR band at 2185 cm^{-1} was ascribed to the CO interacting with the Lewis acid sites (CO-Zr(OH)(OSi)_3), while the band at 2156 cm^{-1} was attributed to CO adsorption on silanols, and the band observed at 2136 cm^{-1} was assigned to pseudoliquid CO vibrations.^{41,42} Obviously, over 16%Zr/MFI(NS), abundant Zr(OH)(OSi)_3 exists and provides Lewis acid sites for the ETB reaction. However, nearly no such Lewis sites were formed on 4%Zr/MFI(NS), in line with its inert activity for ETB.

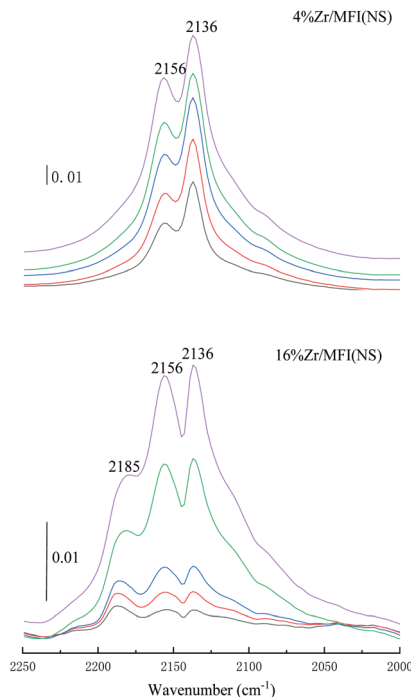


Fig. 7 FTIR spectra of CO adsorbed on the Zr-based catalysts with increased CO pressure.

Introducing 1.2 wt% Mg onto 16%Zr/MFI(NS) decreased the strength of acid sites. As shown in the NH_3 -TPD profiles (Fig. 5), the desorption peak of NH_3 decreased from 141 °C to 116 °C in the presence of Mg. On the other hand, the number of Lewis acid sites slightly increased at the expense of Brønsted acid sites (Table 4). Therefore, more abundant Lewis acid sites with fewer Brønsted sites over the Mg-Zr/MFI(NS) catalyst account for the outstanding catalytic performance in the ETB reaction.

The location of Mg on 1.2%Mg-16%Zr/MFI(NS) was probed by conditional experiments. An organic precursor of Mg (magnesium acetylacetonate) was used to load Mg onto 16%Zr/MFI(NS). Since the molecular size of the organic Mg compound (three times the size of benzene) is larger than the micropore size of MFI(NS), the Mg species would largely remain on the walls of the mesopores without entering into the micropores. From the NH_3 -TPD profile, it can be found that the organic Mg modified catalyst has stronger acidity than the counterpart (131 vs. 116 °C). Quantity analysis according to the Py-IR spectra shows that these two catalysts had similar numbers of Lewis acid sites, but there were more Brønsted acid sites on the 1.2%Mg-16%Zr/MFI(NS)_(organic Mg) catalyst as shown in Table 4. The as-prepared catalyst showed inferior performance to that of 1.2%Mg-16%Zr/MFI(NS), as shown in Table 2, entry 9. Therefore, it can be conjectured that Mg species over the 1.2%Mg-16%Zr/MFI(NS) catalyst have entered the mesopores and micropores. The nanosheets of MFI(NS) provide the catalyst with mesopores and micropores, both of which can host the active sites for the ETB reaction and

endow the hierarchical-structure catalysts with outstanding performance.

3.5.3 Structure of the spent catalyst. The structure stability of the spent catalyst was probed. From SEM and TEM images (Fig. S6 and S7[†]), the morphology of 1.2%Mg–16%Zr/MFI (NS) was well retained after a 7 day run. However, from the XRD patterns (Fig. S8[†]), it can be noticed that besides peaks belonging to the crystalline structure of MFI(NS) zeolite, a new sharp peak appeared, which is attributed to SiO₂ (JCPDS File No. 01-088-2487). This suggests that MFI(NS) is not essentially stable under the reaction conditions. After a long time run, the silica-based support will be gradually changed into crystallized SiO₂ under the *in situ* treatment of steam which is generated during the reaction. It is necessary to improve the structure stability in future studies.

4. Conclusions

A series of Mg–Zr/MFI(NS) catalysts were prepared by a wet impregnation method for the two-step conversion of ethanol to 1,3-BD. According to the catalyst characterization, MFI(NS) is a superior support to highly disperse Zr as compared with the microporous MFI and conventional mesoporous SiO₂. The introduced Zr species preferentially occupy the silanol nests of MFI(NS), eliminating the Brønsted sites at low loadings of Zr and producing abundant weak Lewis acid sites in the form of Zr(OH)(OSi)₃ at high Zr loadings. Over 16%Zr/MFI(NS), 42.3% 1,3-BD selectivity and 60.5% total conversion of ethanol and acetaldehyde were obtained. Introducing 1.2 wt% Mg to 16% Zr/MFI(NS) enhanced the 1,3-BD selectivity to 54.7% with slight depression of the catalytic activity. Mg sites have negligible activity in the MPVO reaction and a certain activity in aldol condensation of acetaldehyde, both of which are much inferior to that of Lewis acid sites. The major function of Mg species in the catalyst should be decreasing the number of Brønsted acid sites so that contributes to 1,3-BD formation. The reaction conditions have remarkable influence on the reaction results. At optimal reaction conditions of 350 °C, a WHSV of 1.44 h⁻¹ and a 2 : 1 ratio of ethanol to acetaldehyde, the 1,3-BD selectivity reached 74.6% with 41.5% of total conversion over 1.2%Mg–16%Zr/MFI(NS), which was maintained for 7 days (168 h) without deactivation. Such high performance of 1.2%Mg–16%Zr/MFI(NS) should be attributed to the abundant weak Lewis acid sites and their high availability in the meso- and micro-pores without Brønsted acid sites. This study demonstrates that the zeolite nanosheet catalysts may have distinguished advantages for the two-step ETB process. The hydrothermal stability of MFI(NS) should be further improved in view of the detrimental effect from the water byproduct during the reaction.

Conflicts of interest

There are no conflicts to declare.

Acknowledgements

This work was supported by the National Natural Science Foundation of China (21690081, 21690084, 21721004 and 21776268) and “Transformational Technologies for Clean Energy and Demonstration”, Strategic Priority Research Program of the Chinese Academy of Sciences (No. XDA 21060200).

Notes and references

- 1 E. V. Makshina, M. Dusselier, W. Janssens, J. Degreve, P. A. Jacobs and B. F. Sels, *Chem. Soc. Rev.*, 2014, **43**, 7917–7953.
- 2 S. Da Ros, M. D. Jones, D. Mattia, J. C. Pinto, M. Schwaab, F. B. Noronha, S. A. Kondrat, T. C. Clarke and S. H. Taylor, *ChemCatChem*, 2016, **8**, 2376–2386.
- 3 G. Pomalaza, M. Capron, V. Ordonsky and F. Dumeignil, *Catalysts*, 2016, **6**, 203–238.
- 4 J. Sun and Y. Wang, *ACS Catal.*, 2014, **4**, 1078–1090.
- 5 G. M. Cabello González, R. Murciano, A. L. Villanueva Perales, A. Martínez, F. Vidal-Barrero and M. Campoy, *Appl. Catal., A*, 2019, **570**, 96–106.
- 6 W. Janssens, E. V. Makshina, P. Vanelderden, F. De Clippel, K. Houthoofd, S. Kerkhofs, J. A. Martens, P. A. Jacobs and B. F. Sels, *ChemSusChem*, 2015, **8**, 994–1008.
- 7 Z. Zhao, K. Chong, J. Jiang, K. Wilson, X. Zhang and F. Wang, *Renewable Sustainable Energy Rev.*, 2018, **97**, 580–591.
- 8 J. Sun and Y. Wang, *ACS Catal.*, 2014, **4**, 1078–1090.
- 9 D. Cespi, F. Passarini, I. Vassura and F. Cavani, *Green Chem.*, 2016, **18**, 1625–1638.
- 10 C. Wang, M. Zheng, X. Li, X. Li and T. Zhang, *Green Chem.*, 2019, **21**, 1006–1010.
- 11 G. Pomalaza, M. C. G. Vofo and F. Dumeignil, *Green Chem.*, 2018, **20**, 3203–3209.
- 12 M. Choi, K. Na, J. Kim, Y. Sakamoto, O. Terasaki and R. Ryoo, *Nature*, 2009, **461**, 246–249.
- 13 V. L. Sushkevich, I. I. Ivanova and V. V. Ordonsky, *ChemSusChem*, 2013, **7**, 2527–2536.
- 14 V. L. Sushkevich, I. I. Ivanov and E. Taarning, *Green Chem.*, 2015, **17**, 2552–2559.
- 15 J. L. Cheong, Y. Shao, S. J. R. Tan, Y. Zhang and S. S. Lee, *ACS Sustainable Chem. Eng.*, 2016, **4**, 4887–4894.
- 16 K. Góra-Marek, K. Tarach and M. Choi, *J. Phys. Chem. C*, 2014, **118**, 12266–12274.
- 17 E. Verheyen, C. Jo, M. Kurttepe, G. Vanbutsele, E. Gobechiya, T. I. Korányi, S. Bals, G. Van Tendeloo, R. Ryoo, C. E. A. Kirschhock and J. A. Martens, *J. Catal.*, 2013, **300**, 70–80.
- 18 M. Zhang and Y. Yu, *Ind. Eng. Chem. Res.*, 2013, **52**, 9505–9514.
- 19 B. Tang, W. Dai, G. Wu, N. Guan, L. Li and M. Hunger, *ACS Catal.*, 2014, **4**, 2801–2810.

- 20 B. Tang, W. Dai, X. Sun, G. Wu, N. Guan, M. Hunger and L. Li, *Green Chem.*, 2015, **17**, 1744–1755.
- 21 W. Dai, S. Zhang, Z. Yu, T. Yan, G. Wu, N. Guan and L. Li, *ACS Catal.*, 2017, **7**, 3703–3706.
- 22 M. Boronat, A. Corma and M. Renz, *J. Phys. Chem. B*, 2006, **110**, 21168–21174.
- 23 A. Corma, M. E. Domine, L. Nemeth and S. Valencia, *J. Am. Chem. Soc.*, 2001, **124**, 3194–3195.
- 24 F. J. Urbano, M. A. Aramendía, A. Marinas and J. M. Marinas, *J. Catal.*, 2009, **268**, 79–88.
- 25 A. Corma, *J. Catal.*, 2003, **215**, 294–304.
- 26 J. He, X. Yang, D. G. Evans and X. Duan, *Mater. Chem. Phys.*, 2002, **77**, 270–275.
- 27 J. V. Ochoa, C. Bandinelli, O. Vozniuk, A. Chierogato, A. Malmusi, C. Recchi and F. Cavani, *Green Chem.*, 2016, **18**, 1653–1663.
- 28 A. Klein and R. Palkovits, *Catal. Commun.*, 2016, **7**, 92–95.
- 29 A. Klein, K. Keisers and R. Palkovits, *Appl. Catal., A*, 2016, **514**, 192–202.
- 30 C. Angelici, M. E. Z. Velthoen, B. M. Weckhuysen and P. C. A. Bruijninx, *Catal. Sci. Technol.*, 2015, **5**, 2869–2879.
- 31 C. Angelici, F. Meirer, A. M. J. van der Eerden, H. L. Schaink, A. Goryachev, J. P. Hofmann, E. J. M. Hensen, B. M. Weckhuysen and P. C. A. Bruijninx, *ACS Catal.*, 2015, **5**, 6005–6015.
- 32 S.-H. Chung, C. Angelici, S. O. M. Hinterding, M. Weingarh, M. Baldus, K. Houben, B. M. Weckhuysen and P. C. A. Bruijninx, *ACS Catal.*, 2016, **6**, 4034–4045.
- 33 V. V. Ordonsky, V. L. Sushkevich and I. I. Ivanova, *J. Mol. Catal. A: Chem.*, 2010, **333**, 85–93.
- 34 C. Angelici, B. M. Weckhuysen and P. C. A. Bruijninx, *ChemSusChem*, 2013, **6**, 1595–1614.
- 35 Y. Xu, Z. Liu, Zheng Han and M. Zhang, *RSC Adv.*, 2017, **7**, 7140–7149.
- 36 Q. Zhu, B. Wang and T. Tan, *ACS Sustainable Chem. Eng.*, 2016, **5**, 722–733.
- 37 X. Gao, J. L. G. Fierro and I. E. Wachs, *Langmuir*, 1999, **15**, 3169–3178.
- 38 Bharat L. Newalkar, Johnson Olanrewaju and Sridhar Komarneni, *J. Phys. Chem. B*, 2001, **105**, 8356–8360.
- 39 Y. Tang, E. Zong, H. Wan, Z. Xu, S. Zheng and D. Zhu, *Microporous Mesoporous Mater.*, 2012, **155**, 192–200.
- 40 Y. Meng, H. C. Genuino, C. H. Kuo, H. Huang, S. Y. Chen, L. Zhang, A. Rossi and S. L. Suib, *J. Am. Chem. Soc.*, 2013, **135**, 8594–8605.
- 41 V. L. Sushkevich, D. Palagin and I. I. Ivanova, *ACS Catal.*, 2015, **5**, 4833–4836.
- 42 V. L. Sushkevich, A. Vimont, A. Travert and I. I. Ivanova, *J. Phys. Chem. C*, 2015, **119**, 17633–17639.